TET1 drives global DNA demethylation via DPPA3-mediated inhibition of maintenance methylation

Christopher B. Mulholland[1], Joel Ryan[1†], Weihua Qin[1†], Michael D. Bartoschek[1†], Franziska R. Traube[2], Edris Parsa[2], Miha Modic[4], Daniel Nixdorf[1], Christoph Ziegenhain[3], Thomas Carell[2], Wolfgang Enard[3], Sebastian Bultmann*[1§] and Heinrich Leonhardt*[1§]

[1]Department of Biology II and Center for Integrated Protein Science Munich (CIPSM), Human Biology and BioImaging, Ludwig-Maximilians-Universität München, Planegg-Martinsried, Germany

[2]Center for Integrated Protein Science (CIPSM) at the Department of Chemistry, Ludwig-Maximilians-Universität München, Munich, Germany

[3]Department of Biology II, Anthropology and Human Genomics, Ludwig-Maximilians-Universität München, Planegg-Martinsried, Germany

[4]The Francis Crick Institute and University College London, Institute of Neurology, London, United Kingdom

[†]These authors contributed equally

§These authors jointly supervised this work

*Correspondence and requests for material should be addressed to S.B. (bultmann@bio.lmu.de) or H.L. (h.leonhardt@lmu.de)

SUMMARY:

DNA modifications undergo genome-wide changes during development, play a central role in epigenetic gene regulation, and preserve genome stability. Ten-eleven translocation (TET) proteins catalyze the oxidation of 5-methylcytosine (5mC) and are implicated in DNA demethylation and the regulation of gene expression (Chen et al., 2013; Ficz et al., 2011; Ito et al., 2011; Khoueiry et al., 2017; Koh et al., 2011; Pfaffeneder et al., 2011; Szwagierczak et al., 2010; Tahiliani et al., 2009; Vella et al., 2013; Williams et al., 2011; Wu et al., 2011; Xiong et al., 2016). However, the degree to which the gene regulatory effects of TET proteins depend on catalytic functions and the extent to which oxidative cytosine modifications represent intermediates of active DNA demethylation or serve as stable epigenetic marks still remains unclear. Here, we dissect the stage-specific catalytic and non-catalytic contributions of TET1 to the regulation of the methylome and transcriptome in the transition from naïve to primed pluripotency. Whereas non-catalytic functions of TET1 prevent the premature exit from pluripotency, we find that the catalytic activity of TET1 is necessary for the expression of the naïve pluripotency marker DPPA3 (STELLA/PGC7)(Hayashi et al., 2008). DPPA3 in turn binds and displaces UHRF1 from nuclear methylation sites to the cytoplasm, thereby impairing the recruitment and activity of the maintenance DNA methyltransferase DNMT1. Collectively, our work delineates catalytic and non-catalytic functions of TET1, uncovers the mechanism of TET1-governed DNA demethylation, and reveals the mechanistic basis by which DPPA3 antagonizes global DNA methylation.

MAIN

To dissect the catalytic and non-catalytic functions of TET1 on transcription and DNA methylation in naïve and primed pluripotency, we generated isogenic *Tet1* catalytic mutant (T1CM) mouse embryonic stem cell (ESC) lines (Extended Data Figure 1a-d) and compared them with our previously established *Tet1* knockout (T1KO) ESCs (Mulholland et al., 2018). To this end, we first differentiated naïve wild-type and *Tet1* mutant ESCs into primed, epiblast-like cells (EpiLCs)(Hayashi et al., 2011) and monitored the transcriptome and methylome with RNA-seq and reduced representation bisulfite sequencing (RRBS), respectively.

Figure 1: TET1 catalytic activity is required to prevent the premature acquisition of DNA methylation.

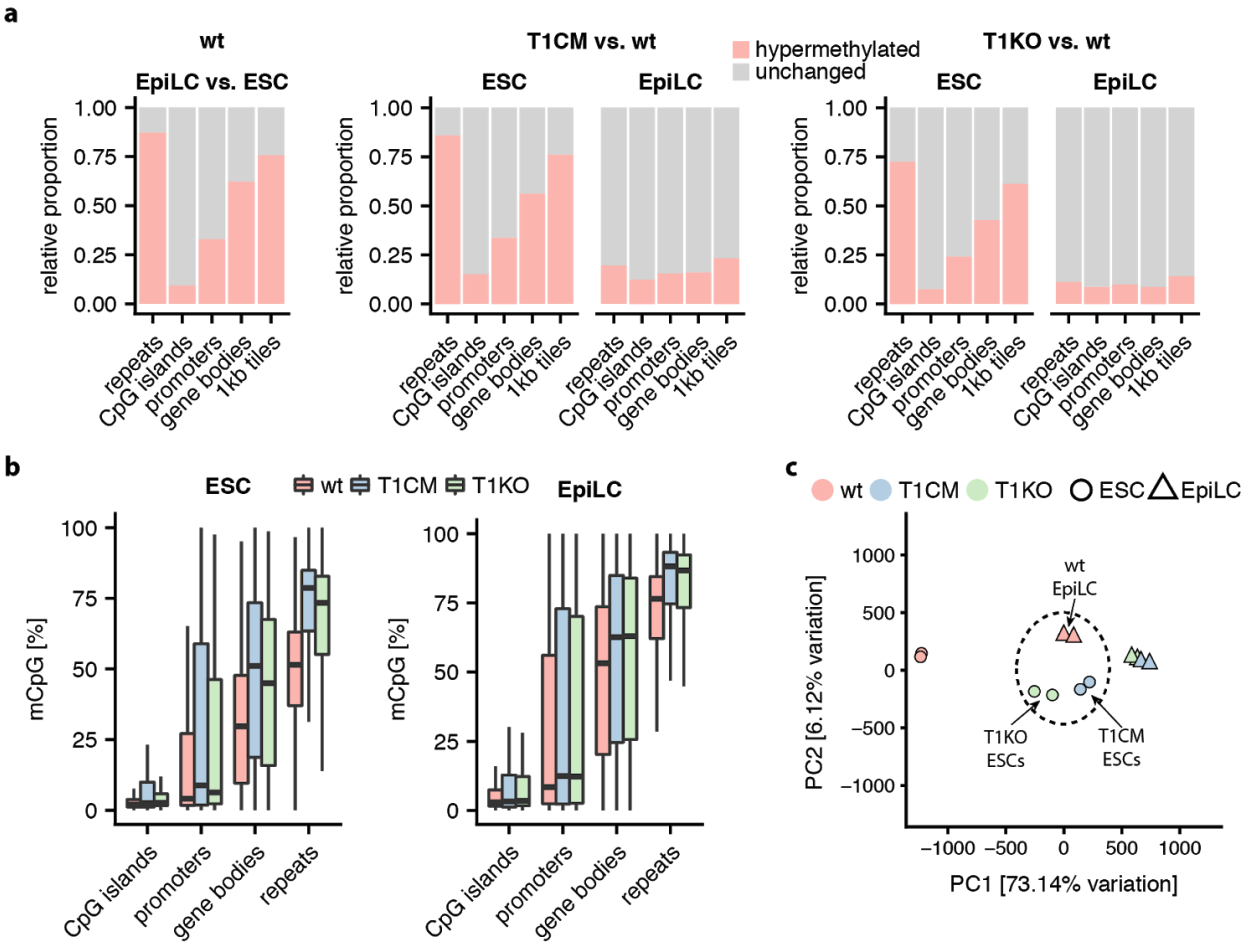

Figure 1: TET1 catalytic activity is required to prevent the premature acquisition of DNA methylation. a) Relative proportion of DNA hypermethylation (q value < 0.05; absolute methylation difference > 20%), for each element in wild-type (wt) cells during differentiation (left panel) as well as in *Tet1* catalytic mutant (T1CM) or *Tet1* knockout (T1KO) compared to wt ESCs or EpiLCs (middle and right panels). b) Box plots depicting percentage of CpG methylation at CpG islands, promoters, gene bodies, and repeats for wt, T1CM, and T1KO at the ESC (left panel) and EpiLC (right panel) stage. c) Principal component (PC) analysis of wt, T1CM, and T1KO reduced representation bisulfite sequencing (RRBS) data during EpiLC differentiation. Circles represent ESC samples and

triangles represent EpiLC samples. Details for all figures regarding sample sizes and how samples were collected can be found in Methods 'Statistics and reproducibility' section.

Analysis of RRBS data from wild-type cells presented the previously described global increase in DNA methylation during the transition from naïve to primed pluripotency (Figure 1a and Extended Data Figure 2a-b)(Ficz et al., 2013; Habibi et al., 2013; Pfaffeneder et al., 2014). Comparison of RRBS data from T1KO and T1CM with wild-type ESCs and EpiLCs revealed significant DNA hypermethylation at both stages, especially at promoters, gene bodies, and repetitive elements (Figure 1a). Hypermethylation was particularly pronounced in T1KO and T1CM ESCs, which displayed DNA methylation levels similar to those of wild-type EpiLCs (Figure 1b). As global hypermethylation is a hallmark of the naïve to primed transition, we applied a principal component analysis to our RRBS data (Figure 1c). Whereas wild-type ESCs and EpiLCs clearly separated in PC1 (~73% explained variation), ESCs and EpiLCs from TET1 mutants clustered closer to wild-type EpiLCs. Accordingly, the vast majority of significantly hypermethylated promoters and gene bodies in both T1KO and T1CM ESCs overlapped with those gaining DNA methylation during the exit from naïve pluripotency in wild-type cells (Extended Data Figure 2c-d). We observed a similar phenomenon at repetitive elements, which comprise most of the genome. The majority of detected repeat subclasses including LINE, LTR, and SINE elements were significantly hypermethylated in both T1KO and T1CM ESCs. Again, this trend mirrored the methylation gains of these repetitive elements during the transition of wild-type ESCs to EpiLCs (Extended Data Figure 2e). In summary, these results show that TET1 catalytic activity is required to ensure the integrity of the naïve methylome by preventing the premature acquisition of a primed methylation signature.

We next examined whether the premature acquisition of DNA methylation in T1KO and T1CM ESCs can be explained by a premature exit from naïve pluripotency in these mutants. Therefore, we measured expression profiles using RNA-seq in wild-type and mutant ESCs and EpiLCs. We found that expression differences between ESCs and EpiLCs in wild-type (1670 significant genes) are highly similar to the expression differences between ESCs and EpiLCs in TET1 mutants, as illustrated by the strong clustering by differentiation state (Figure 2a). This indicates that neither loss of TET1 nor loss of its catalytic activity causes premature commitment of ESCs towards EpiLCs and suggests that TET1-dependent DNA methylation and transcription are largely uncoupled during the transition from naïve to primed pluripotency.

Although loss of TET1 did not cause premature commitment towards EpiLCs, T1KO cells exhibited transcriptional up- as well as downregulation in similar proportions at both cellular stages, in line with TET1's reported dual role in transcriptional regulation (Wu et al., 2011) (Figure 2b and Extended Data Figure 3a). Surprisingly, the catalytic activity is largely dispensable for transcriptional regulation as T1CM cells displayed compared to T1KO cells only 130 (vs. 431) and 157 (vs. 646) differentially

expressed genes in ESCs and EpiLCs, respectively (Figure 2c). This observation was particularly unexpected considering that both loss of TET1 or its catalytic activity resulted in highly similar DNA hypermethylation phenotypes.

Intrigued by this finding, we examined the relationship between transcriptional changes in T1KO and T1CM cells in more detail. To focus on *bona fide* TET1 transcriptional targets, we used publicly available TET1 ChIP-seq data to limit our analysis of differentially expressed genes in T1KO or T1CM ESCs and EpiLCs to those bound by TET1 (Extended Data Figure 3b)(Khoueiry et al., 2017; Xiong et al., 2016). We then performed unsupervised hierarchical clustering on this subset, allowing us to precisely define catalytic and non-catalytic targets of TET1 at both developmental stages (Figure 2d and e). In agreement with the global analysis (Figure 2b and c), the catalytic activity of TET1 is dispensable for the regulation of the majority of its transcriptional targets at both stages, with only ~27% and ~39% of genes identified as catalytically dependent in ESCs and EpiLCs, respectively. Moreover, this analysis revealed that naïve pluripotency markers are specifically repressed by the catalytic activity of TET1 whereas in EpiLCs non-catalytic functions prevent the premature activation of lineage markers (Extended Data Figure 3c).

To further investigate how the catalytic and non-catalytic roles of TET1 govern the pluripotency breakdown and transition towards differentiation progeny, we generated T1KO and T1CM mutants in a reporter ESC line (Extended Data Figure 4a,b), in which *Brachyury* (also known as *T*) endogenously fused to eGFP indicates primitive streak commitment (Fehling et al., 2003). In contrast to the wild-type and T1CM, we observed the T1KO to prematurely induce the formation of primitive streak progenitors during prolonged EpiLC culture (Extended Data Figure 3e) demonstrating that primarily non-catalytic functions of TET1 contribute to its reported role in preventing precocious lineage commitment (Williams et al., 2011; Wu et al., 2011). To probe the consequence of the upregulated naïve pluripotency network (Extended Data Figure 3c) upon loss of TET1 catalytic activity, we performed an SSEA-1 staining after 72 h of differentiation and observed the persistence of a significant population of naïve pluripotent cells in both T1KO and T1CM cultures, in contrast to wild-type cultures (Extended Data Figure 3d). Of note, *Tet1* was recently detected in a genetic screen for factors involved in the exit from naïve pluripotency (Leeb et al., 2014). In conclusion, our results demonstrate TET1 to have opposing roles in the exit of pluripotency and lineage commitment, which are regulated not only in a stage-specific manner but also by distinct modes of action.

We next examined promoter methylation levels at catalytic dependent and independent genes. All clusters displayed only slight changes in promoter methylation (Figure 2f) with only a small fraction (~4.3% - 9.5%) of differentially expressed genes exhibiting differential promoter methylation in ESCs or EpiLCs. Furthermore, hypermethylation and transcriptional repression were not correlated at either

pluripotency stage (Extended Data Figure 3f). This disparity was reflected in the differing promoter CpG compositions of differentially expressed genes (predominantly high CpG content) and differentially methylated promoters (intermediate and low CpG content) (Extended Data Figure 3g-h). Using publicly available data (Khoueiry et al., 2017), we found a strong enrichment of 5-hydroxymethylcytosine (5hmC) at promoters within catalytic dependent clusters compared to catalytic independent clusters (Figure 2g). Taken together, these findings suggest that TET1 transcriptionally regulates genes dependent on its catalytic activity by maintaining adequate promoter 5hmC levels, as opposed to protecting promoters from 5-methylcytosine (5mC) accumulation.

In contrast to differentially expressed genes, the most dramatic DNA methylation changes were detected at promoters with unchanged transcriptional activity in T1KO ESCs and EpiLCs, and consisted mostly of genes with either low or undetectable expression (Extended Data Figure 5a). This finding prompted us to investigate whether the distinct transcriptional deregulation and differential methylation correlate with TET1 occupancy. Whereas TET1 strongly bound promoters of transcriptionally deregulated genes, TET1 was not enriched at differentially methylated promoters in ESCs or EpiLCs (Figure 3a and Extended Data Figure 5a). Moreover, throughout the genome TET1 occupancy was significantly lower at differentially methylated sites than at sites of unchanged 5mC occupancy (Figure 3b). Taken together, these results raise the question whether the observed DNA hypermethylation in T1KO and T1CM cells is caused by indirect effects.

Figure 2: Catalytic and non-catalytic functions of TET1 do not involve promoter demethylation.

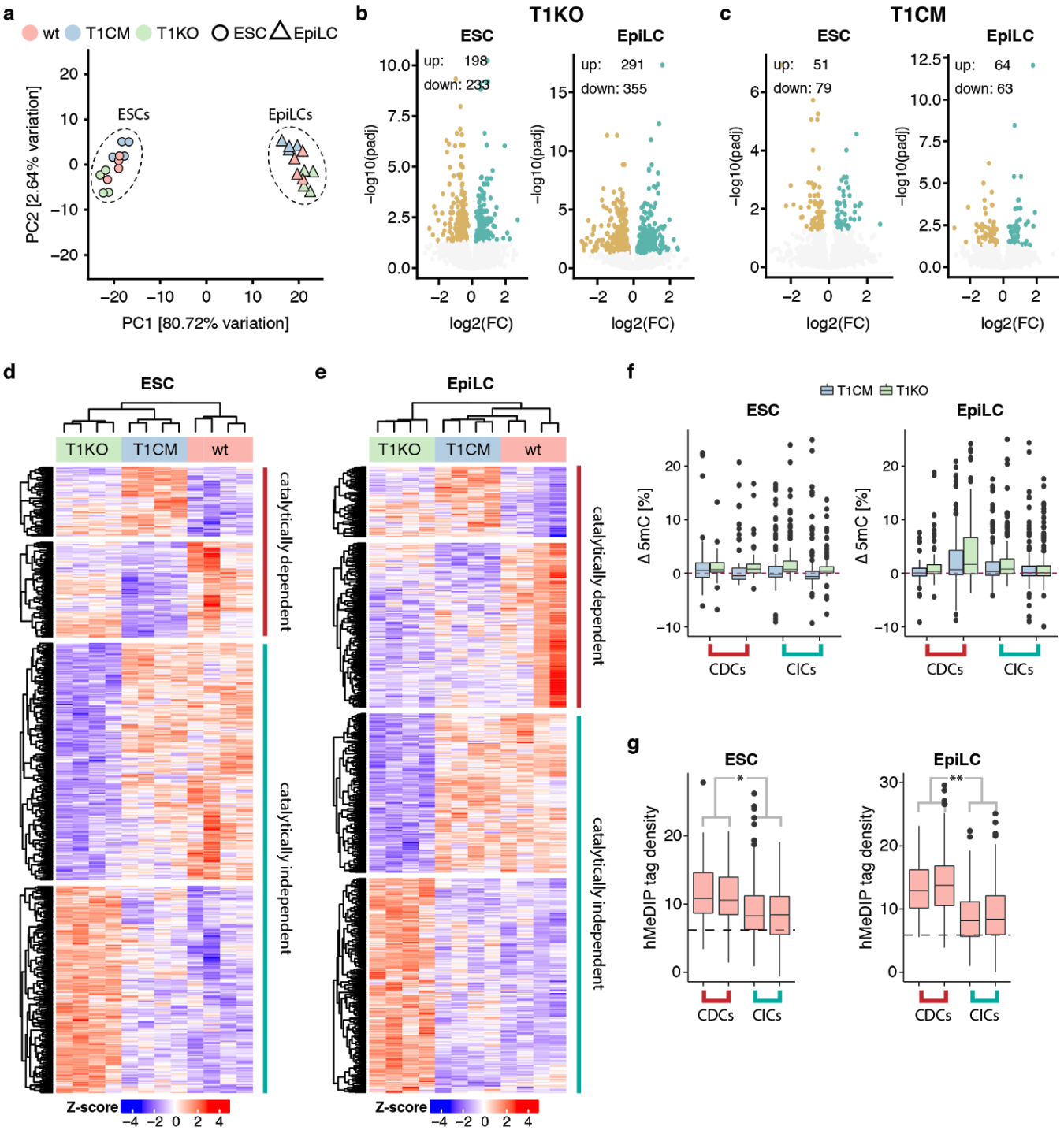

Figure 2: Catalytic and non-catalytic functions of TET1 do not involve promoter demethylation. a) Principal component (PC) analysis of wild-type (wt), *Tet1* catalytic mutant (T1CM), and *Tet1* knockout (T1KO) RNA-seq data during EpiLC differentiation. PC analysis was performed on genes that are differentially expressed during differentiation of wt cells (n = 1670). Circles represent ESC samples and triangles represent EpiLC samples. b,c) Volcano plots depicting fold change in gene expression and their significance in T1KO (b) and T1CM (c) relative to wt ESCs (left panel) and EpiLCs (right panel). Numbers of differentially expressed genes (adjusted p-value <

0.05) at each stage are indicated. d,e) Hierarchical clustering of differentially expressed genes in ESCs (d) and EpiLCs (e) of wt, T1CM, and T1KO cells. Catalytically dependent clusters are defined by changes in both T1KO and T1CM cells compared to wt. Catalytically independent clusters exhibit changes in T1KO cells only. f) Box plots depicting changes in promoter DNA methylation (%) of T1CM and T1KO cells compared to wt for catalytically dependent clusters (CDCs) and catalytically independent clusters (CICs) in ESCs (left panel) and EpiLCs (right panel). g) 5-hydroxymethylcytosine (5hmC) levels determined by hMeDIP (Khoueiry et al., 2017) at promoters within CDCs and CICs in wt ESCs (left panel) and EpiLCs (right panel). Welch two-sided t-test: * $P<0.05$; ** $P<0.01$.

Therefore, we first examined potential transcriptional deregulation of known members of the DNA methylation machinery but detected no change in the expression of *Dnmt1*, *Uhrf1*, *Dnmt3a*, and *Dnmt3b* in T1KO or T1CM ESCs and EpiLCs (Extended Data Figure 5b,c). To unbiasedly determine gene expression changes associated with global DNA hypermethylation, we performed differential expression analysis comparing the transcriptomes of hypomethylated cells (wt ESCs) and hypermethylated cells (wt EpiLCs, T1KO and T1CM ESCs as well as EpiLCs). Most strikingly, *Dppa3* expression (also known as *Stella* and *Pgc7*) was significantly reduced in hypermethylated cell lines (Extended Data Figure 5e). In particular, *Dppa3* transcript levels were downregulated in T1KO as well as T1CM cells indicating that its expression is dependent on the catalytic activity of TET1 (Figure 3c). To gain mechanistic insights into the TET1-mediated regulation of *Dppa3*, we analyzed TET1 occupancy and 5hmC levels at the *Dppa3* locus. TET1 was found to bind ~1.7kb upstream of *Dppa3*, a region reported to function as a transcriptional enhancer for *Dppa3* expression (Waghray et al., 2015). This binding site exhibits enriched 5hmC occupancy which markedly declines upon loss of TET1, further supporting a central role of TET1 catalytic activity in regulating *Dppa3* expression (Extended Data Figure 5d).

DPPA3 was shown to protect imprinted loci and retrotransposons from DNA demethylation during fertilization as well as primordial germ cell development (Nakamura et al., 2007; Nakashima et al., 2013). In striking contrast, ectopic expression of *Dppa3* was reported to inhibit maintenance DNA methylation in somatic cells (Funaki et al., 2014). These conflicting reports prompted us to explore the function of DPPA3 during the exit from naïve pluripotency. Therefore, we first established isogenic *Dppa3* knockout (Dppa3KO) mouse ESCs using CRISPR/Cas (Extended Data Figure 6a-c). To assess DNA methylation levels, we applied a targeted bisulfite sequencing approach, which provides DNA methylation levels for ~1.5e4 CpGs in LINE-1 elements (Extended Data Figure 7). Strikingly, loss of DPPA3 in ESCs resulted in a dramatic increase of 5mC levels at LINE-1 elements exceeding even the hypermethylation observed in T1CM ESCs (Figure 3d). Moreover, liquid chromatography coupled with mass spectrometry (LC–MS/MS) revealed a significant global increase in 5mC levels in Dppa3KO comparable to T1CM ESCs (Figure 3e). To exclude that global DNA hypermethylation upon loss of

DPPA3 was a consequence of *Tet* downregulation, we measured *Tet1*, *Tet2*, and *Tet3* transcript levels in Dppa3KO ESCs. Compared to wt, *Tet1* levels remained constant and *Tet2* levels increased in line with significantly elevated 5hmC levels (Figure 3e and Extended Data Figure 5f). To compare the hypermethylation caused by loss of TET1 and DPPA3 at single-base resolution we performed RRBS on Dppa3KO ESCs. Strikingly, the overlap of hypermethylated CpGs among Dppa3KO, T1KO, and T1CM ESCs was 74%, indicating that the majority of hypermethylation in TET1 mutant cells can be explained by a loss of DPPA3 (Figure 3f). To determine whether hypermethylation in T1CM cells is in fact a direct consequence of *Dppa3* downregulation, we rescued DPPA3 levels by stably introducing a doxycycline inducible *Dppa3* expression cassette into T1CM as well as wild-type cells (Extended Data Figure 8a-c). Expression of DPPA3 effectively rescued the observed hypermethylation phenotype at LINE-1 elements in T1CM ESCs, and prolonged induction of *Dppa3* even resulted in LINE-1 hypomethylation in wild-type ESCs (Figure 3g). Collectively, these results show that the majority of demethylation attributed to TET1 catalytic activity in naïve pluripotency is not the result of active demethylation but an indirect result of TET1-mediated 5mC oxidation promoting *Dppa3* transcription.

Figure 3: TET1 maintains global DNA methylation levels indirectly via the regulation of *Dppa3*

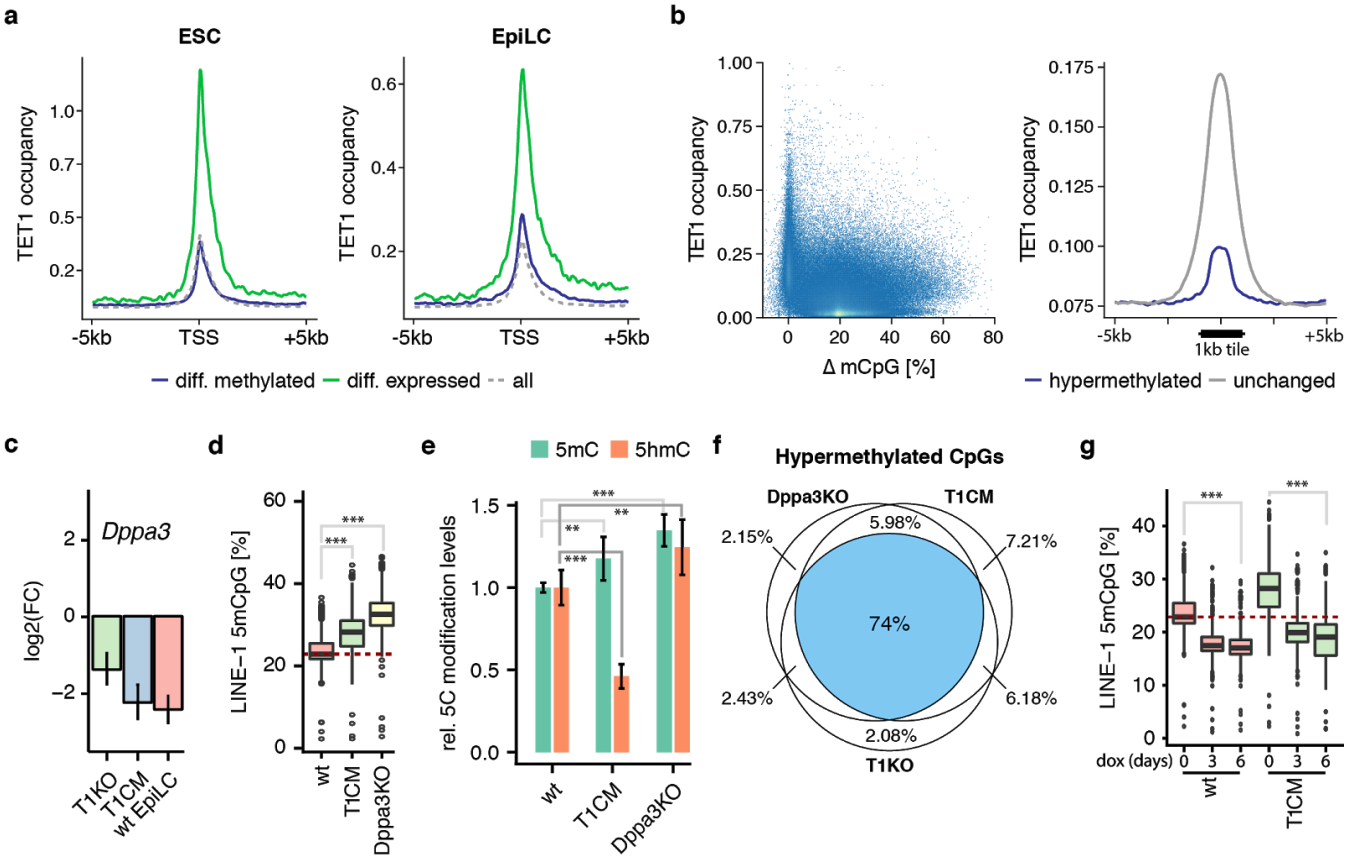

Figure 3: TET1 maintains global DNA methylation levels indirectly via the regulation of *Dppa3*. a) TET1 occupancy (Khoueiry et al., 2017; Xiong et al., 2016) at transcriptional start sites (TSS) of differentially expressed (green), differentially methylated (blue), and all promoters in wild-type (wt) ESCs (left panel) and EpiLCs (right

panel). Differentially expressed or methylated promoters: TET1 knockout (T1KO) vs. wt ESCs or EpiLCs, respectively. b) Scatter plot depicting TET1 occupancy in wt and changes in DNA methylation in TET1 catalytic mutant (T1CM) ESCs at all genomic 1kb tiles detected by reduced representation bisulfite sequencing (RRBS) (left panel). TET1 occupancy at differentially methylated (blue) and unchanged (grey) 1kb tiles (right panel). c) Fold change (FC) of *Dppa3* expression in T1KO ESCs, T1CM ESCs, and wt EpiLCs relative to wt ESCs. Error bars indicate standard error. d) DNA methylation levels at LINE-1 elements (%) in wt, T1CM, and *Dppa3* knockout (Dppa3KO) ESCs as measured by targeted bisulfite sequencing. e) Relative cytosine (5C) modification levels for 5-methylcytosine (5mC) and 5-hydroxymethylcytosine (5hmC) in wt, T1CM, and Dppa3KO ESCs as measured by mass spectrometry (LC-MS/MS). Error bars indicate standard deviation. f) Overlap of hypermethylated CpGs in T1CM, T1KO, and Dppa3KO ESCs determined by RRBS. g) DNA methylation levels at LINE-1 elements (%) as measured by targeted bisulfite sequencing in wt and T1CM ESCs after 0, 3, or 6 days of doxycycline (dox) induction of *Dppa3* expression. d-,g) Welch two-sided t-test: ** P<0.01; *** P<0.001.

We next sought to explore the mechanistic basis by which DPPA3 antagonizes DNA methylation. We hypothesized that the mechanism proceeds via impairment of maintenance methylation, analogous to observations in somatic cells (Funaki et al., 2014). As reduced protein levels of UHRF1, an essential component of the DNA maintenance methylation machinery (Hashimoto et al., 2008; Sharif et al., 2007), are thought to preserve global hypomethylation in naïve pluripotency (von Meyenn et al., 2016), we investigated whether DPPA3 expression influences UHRF1 abundance. UHRF1 protein levels were comparable between wild-type and T1CM ESCs, and not altered by prolonged *Dppa3* induction (Extended Data Figure 8d). To investigate whether DPPA3 influences UHRF1 localization, we generated an endogenous UHRF1-GFP fusion ESC line harboring the inducible *Dppa3* cassette (Extended Data Figure 8a, 9) and tracked the localization of UHRF1-GFP upon *Dppa3* induction in living cells. Astonishingly, forced expression of DPPA3 rapidly disrupted the well-defined subnuclear distribution of UHRF1-GFP and further led to its translocation into the cytoplasm (Figure 4a; Supplementary Video 1). To quantify the redistribution of cellular UHRF1 in an unbiased manner from live-cell time lapse images, we used the spatial autocorrelation function (SACF) to determine fluctuations in the spatial distribution of the fluorescence of UHRF1-GFP over the course of DPPA3 induction (Petersen et al., 1993). Calculation of spatial autocorrelation allowed the extraction of a correlation width at each time point (Extended Data Figure 10a-b)(Görisch et al., 2005), a parameter reflective of the area occupied by fluorescently labeled proteins. Upon DPPA3 induction, the average correlation width rapidly increased from ~4 µm to ~13 µm (Extended Data Figure 10c). When applying the same analysis on uninduced cells, the UHRF1-GFP correlation width remained static (roughly half the size of the nucleus) over the course of the time-lapse (Extended Data Figure 10c), ruling out fluctuations in correlation width due to normal cell proliferation. Thus, the increase in correlation width is indicative of the UHRF1-GFP signal extending and persisting beyond the nucleus, and a direct consequence of DPPA3 induction.

Whereas UHRF1-GFP prominently decorated the mitotic chromosomes of uninduced cells, the diffuse UHRF1-GFP pattern persisted through mitosis in *Dppa3*-induced cells (Figure 4a; Supplementary Video 1), suggesting DPPA3 directly hinders UHRF1 binding. Indeed, UHRF1-GFP mobility as assessed by Fluorescence Recovery After Photobleaching (FRAP) dramatically increased after DPPA3 induction, indicative of abrogated chromatin binding (Figure 4e, Extended Data Figure 10d-e). Moreover, co-immunoprecipitation revealed a physical interaction between DPPA3 and UHRF1 (Extended Data Figure 10f), and redistribution of nuclear UHRF1-GFP after *Dppa3* induction correlated with a pronounced enrichment of cytosolic DPPA3 (Figure 4b). To determine whether DPPA3 mediates the cytosolic retention of UHRF1 under physiological conditions, we performed biochemical fractionation on wild-type and Dppa3KO ESC samples. In contrast to cytoplasmic accumulation of UHRF1-GFP upon DPPA3 overexpression (Extended Data 10g), loss of DPPA3 abolished cytoplasmic localization of UHRF1 in naïve Dppa3KO ESCs (Figure 4c). Of note, nuclear exclusion of UHRF1 is only known to occur during pre-implantation development and germline specification, two developmental timeframes during which DPPA3 expression is highest (Maenohara et al., 2017; Sato et al., 2002). In summary, we identify a novel pathway of UHRF1 regulation in naïve pluripotency, in which TET-mediated oxidation controls DPPA3 expression to regulate the subcellular distribution of UHRF1.

Figure 4: DPPA3 antagonizes DNA maintenance methylation

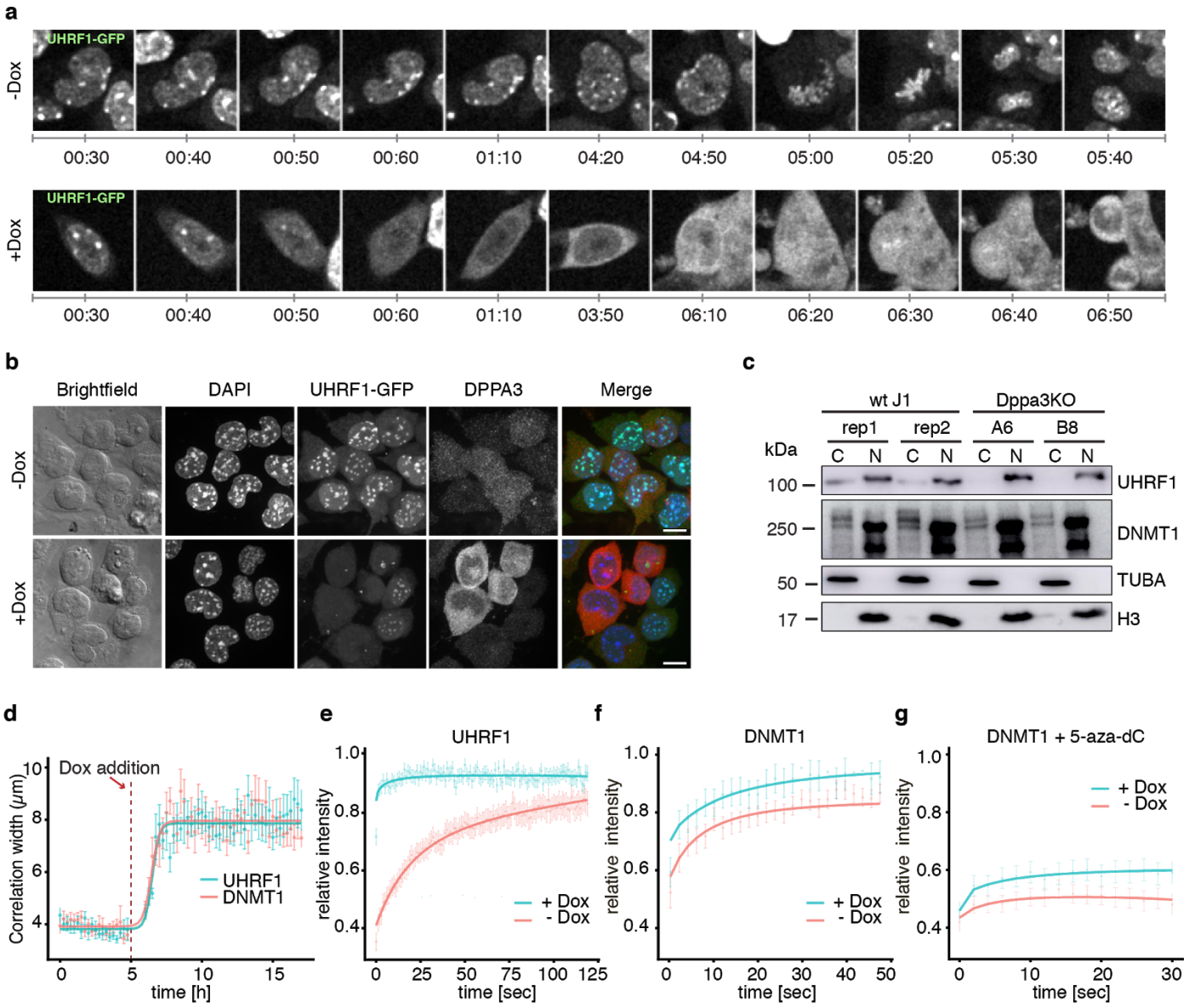

Figure 4: DPPA3 antagonizes DNA maintenance methylation. a) Time lapse imaging of live *Uhrf1*$^{GFP/GFP}$ naïve ESCs harboring an inducible *Dppa3* expression cassette (*Uhrf1*$^{GFP/GFP}$*/SBtet-3xFLAG-Dppa3*) starting 30 min after induction with doxycycline (+Dox). Data acquisition was simultaneously initiated for untreated *Uhrf1*$^{GFP/GFP}$*/SBtet-3xFLAG-Dppa3* naïve ESCs (-Dox). Duration of time lapse imaging is given in hours following doxycycline addition. b) UHRF1-GFP and DPPA3 localization assessed by immunofluorescence in *Uhrf1*$^{GFP/GFP}$*/SBtet-3xFLAG-Dppa3* naïve ESCs in the absence of doxycycline (-Dox) or after 24 h of *Dppa3* induction (+Dox). Gaussian blur (0.3 px) and autocontrast were applied to each channel and condition. Scale bar: 10 µm. c) Western blot analysis of UHRF1 and DNMT1 in fractionated wild-type (wt) J1 and *Dppa3* knockout (Dppa3KO) ESC samples. Fractionation was performed using two independent biological replicates of wt J1 (rep1 and rep2) and Dppa3KO (clone A6 and B8). Cytoplasmic (C) and nuclear (N) fractions were verified with alpha-tubulin (TUBA) and histone H3 (H3) as loading controls, respectively. In contrast to wt J1, UHRF1 is fully retained within the nuclear fraction of Dppa3KO ESCs. d) Kinetics of UHRF1 and DNMT1 redistribution upon

doxycycline treatment depicted as the average correlation width of GFP signal determined at each time point by live cell microscopy of naïve *Uhrf1*$^{GFP/GFP}$*/SBtet-3xFLAG-Dppa3* or *Dnmt1*$^{GFP/GFP}$*/SBtet-3xFLAG-Dppa3* ESCs. Positions imaged per time point: DNMT1 n=11, UHRF1 n=12. e-g) Fluorescence recovery after photobleaching (FRAP) analysis of UHRF1-GFP or GFP-DNMT1 in uninduced (-Dox) naïve *Uhrf1*$^{GFP/GFP}$*/SBtet-3xFLAG-Dppa3* or *Dnmt1*$^{GFP/GFP}$*/SBtet-3xFLAG-Dppa3* ESCs and after 48 h of *Dppa3* induction (+Dox). Solid lines in each plot represent the average fluorescence intensity of *n* cells. e) Measurement of nuclear UHRF1-GFP mobile and immobile fractions (+Dox: n=27; -Dox: n=32). f) GFP-DNMT1 recovery kinetics during S-phase (+Dox: n=14; -Dox: n=20). g) Determination of the catalytically active fraction of DNMT1 during S-phase using the mechanism based inhibitor 5-azadeoxycytidine (5-aza-dC). In this assay, active DNMTs are irreversibly trapped in the covalent complex formation step of 5-cytosine methylation. DNMT1 immobilization is detected as a lack of recovery after photobleaching corresponding to catalytically active DNMT1(Schermelleh et al., 2005) (+Dox: n=19; -Dox: n=26). e-g) Error bars indicate standard error.

As UHRF1 is required for the proper targeting of the maintenance DNA methyltransferase DNMT1 to the replication fork (Bostick et al., 2007; Sharif et al., 2007), we investigated the extent to which DPPA3-mediated UHRF1 redistribution affects this process. Forced expression of DPPA3 resulted in the dramatic depletion of UHRF1-GFP from replication sites in live cells (Extended Data Figure 11a). To determine the consequence of this depletion on DNMT1 targeting, we inserted the inducible *Dppa3* cassette into an endogenous GFP-DNMT1 fusion ESC line (Mulholland et al., 2015). After *Dppa3* induction, GFP-DNMT1 displayed a more diffuse nuclear distribution and, notably, even a detectable cytosolic fraction (Extended Data Figure 11b,c; Supplementary Video 2). Applying spatial autocorrelation analysis, an increased correlation width (-Dox: ~4 µm, +Dox: ~8 µm) confirmed the rapid emergence and persistence of cytoplasmic GFP-DNMT1 in response to DPPA3 (Figure 4d). Moreover, we observed the cellular redistribution of GFP-DNMT1 and UHRF1-GFP upon DPPA3 induction to follow similar kinetics (half maximum: ~1.5 h)(Figure 4d).

Interestingly, DNMT1, like UHRF1, is concentrated in the cytoplasm during early development from the oocyte to the four-cell stage (Carlson et al., 1992), a developmental time frame during which DPPA3 is highly expressed and global DNA demethylation occurs (Nakamura et al., 2007). In line with the substantial defect in UHRF1 localization, GFP-DNMT1 enrichment at replication sites was severely diminished in response to elevated levels of DPPA3 (Extended Data Figure 11b). FRAP analysis revealed increased mobility of S-phase GFP-DNMT1 after ectopic DPPA3 expression (Figure 4f, Extended Data Figure 11d,e), indicating that the reduction of DNMT1 at replication sites is due to impaired chromatin binding. To test whether altered distribution and binding of DNMT1 are also accompanied by reduced enzymatic activity, we repeated GFP-DNMT1 FRAP analysis in the presence of 5-azadeoxycytidine (5-aza-dC), a mechanism based inhibitor that traps catalytically active DNMT1 in the covalent complex formation step of the methylation reaction (Schermelleh et al., 2005). In the absence of doxycycline, GFP-DNMT1 was rapidly immobilized after 5-aza-dC treatment

whereas in cells overexpressing DPPA3 significantly reduced trapping of GFP-DNMT1 was detected (Figure 4g, Extended Data Figure 11f,g). Taken together, DPPA3 compromises UHRF1 binding, disrupts DNMT1 localization, and ultimately reduces the fraction of catalytically active DNMT1, thereby impairing DNA methylation maintenance.

Our study demonstrates that TET1 catalytic activity maintains the hypomethylated naïve DNA methylome not directly via global active DNA demethylation but indirectly via the locus-specific, positive regulation of *Dppa3* by 5mC oxidation. We show that DPPA3 impairs maintenance DNA methylation by altering the subcellular distribution of UHRF1 and DNMT1 thereby compromising the efficiency of DNA methylation maintenance. In line with these findings, earlier studies suggested active DNA demethylation by TET1 during the reprogramming of serum cultured ESCs into naïve, hypomethylated ESCs (Blaschke et al., 2013; Ficz et al., 2013; Habibi et al., 2013) whereas later work established passive DNA demethylation as the major pathway (von Meyenn et al., 2016). Intriguingly, vitamin C was shown to increase the kinetics of global DNA demethylation during this process in a TET1-dependent manner (Blaschke et al., 2013; von Meyenn et al., 2016). Our results unify these seemingly contradicting observations by demonstrating the central role of TET1 catalytic activity in regulating maintenance DNA methylation. Clearly, such passive DNA demethylation is safer than the active removal of 5mC by TDG-mediated base excision repair which requires strand breaks and DNA synthesis. However, passive demethylation is slower and strictly dependent on DNA replication and therefore not possible in all cells. It is attractive to speculate that active demethylation prevails in postmitotic cells and when selected genes are reactivated, whereas passive demethylation is used for genome-wide changes in stem or germline cells, where any repair induced mutation could have severe consequences. Further research is required to clarify how these alternative demethylation pathways are chosen in different cell types and how they contribute to dynamic changes in genome-wide DNA modification patterns.

Collectively, our findings question the role of oxidized cytosine derivatives as intermediates of DNA demethylation on a global scale, emphasize their importance as independent, locus-specific epigenetic marks, and identify a novel pathway for TET-mediated DNA demethylation. This pathway provides a mechanistic link for previously unconnected observations in early embryonic development where the nuclear exclusion of UHRF1(Maenohara et al., 2017; Seisenberger et al., 2012) and DNMT1(Carlson et al., 1992), high TET activity (Amouroux et al., 2016; Hill et al., 2018; Shen et al., 2014), and *Dppa3* expression (Sato et al., 2002) all coincide with passive DNA demethylation.

Acknowledgements

We would like to thank Dr. H. Blum, Dr. S. Krebs (Laboratory for Functional Genome Analysis, LMU Munich), and Dr. A. Brachmann (Faculty of Biology, Department of Genetics, LMU Munich) for next

generation sequencing services. We thank V. Laban, C. Kirschner, P. Stolz, T.J. Fischer, and V.B. Ozan for help with experiments, J. Koch for technical assistance, and Dr. I. Hellmann for advice on data analysis and providing computational infrastructure. We would like to thank Dr. S. Stricker for helpful discussions and constructive criticism on the manuscript. We thank Dr. Feng Zhang for providing the pSpCas9(BB)-2A-Puro (PX459) and SpCas9-T2A-GFP (PX458) (Addgene plasmids #62988 and 48138) plasmids, Dr. Eric Kowarz for the gift of the pSB-tetPur (Addgene plasmid #60507) construct, and Dr. Zsuzsanna Izsvak for the gift of the pCMV(CAT)T7-SB100 (Addgene plasmid # 34879). We are grateful to Dr. Valerie Kouskoff for providing the *Brachyury*$^{GFP/GFP}$ ESCs. J.R. and M.D.B. are fellows of the International Max Planck Research School for Molecular Life Sciences (IMPRS-LS). C.B.M gratefully acknowledges the support of the Fulbright Commission and the late Dr. Glenn Cuomo. F.R.T. thanks the Boehringer Ingelheim Fonds and J.R. the Fonds de Recherche du Québec en Santé for a PhD fellowship. The work was funded by the Deutsche Forschungsgemeinschaft (DFG grants SFB1064/A22 to S.B, SFB1064/A17 and SFB1243/A01 to H.L., and SFB1243/A14 to W.E.).

Authors Contributions

C.B.M. and S.B. designed and conceived the study. S.B. and H.L. supervised the study. C.M., S.B., and H.L. prepared the manuscript with the help of M.D.B.. C.B.M. performed cellular and molecular experiments and generated cell lines with assistance from D.N. C.B.M. performed RRBS and RNA-Seq with help and supervision from C.Z., S.B., and W.E. J.R. and C.B.M. performed live-cell microscopy and photobleaching analyses. M.D.B. helped with cell line validation and performed fluorescence microscopy analysis. W.Q. performed the biochemical analyses. M.M performed FACS experiments. F.R.T. and E.P. quantified modified cytosines by LC-MS/MS with the supervision by T.C. S.B. performed data analysis. All authors read, discussed, and approved the manuscript.

Methods

Cell culture

Naïve J1 mouse ESCs were cultured and differentiated into EpiLCs as described previously (Hayashi and Saitou, 2013; Mulholland et al., 2015). In brief, for both naïve ESCs and EpiLCs defined media was used, consisting of N2B27: 50% neurobasal medium (Life Technologies), 50% DMEM/F12 (Life Technologies), 2 mM L-glutamine (Life Technologies), 0.1 mM β-mercaptoethanol (Life Technologies), N2 supplement (Life Technologies), B27 serum-free supplement (Life Technologies), 100 U/mL penicillin, and 100 µg/mL streptomycin (Sigma). Naïve ESCs were maintained on flasks treated with 0.2% gelatin in defined media containing 2i (1 µM PD032591 and 3 µM CHIR99021 (Axon Medchem, Netherlands)), 1000 U/mL recombinant leukemia inhibitory factor (LIF, Millipore), and 0.3% BSA (Gibco) for at least three passages before commencing differentiation.

To differentiate naïve ESCs into Epiblast-like cells (EpiLCs), flasks were first pre-treated with Geltrex (Life Technologies) diluted 1:100 in DMEM/F12 (Life Technologies) and incubated at 37 °C overnight. Naive ESCs were plated on Geltrex-treated flasks in defined medium containing 10 ng/mL Fgf2 (R&D Systems), 20 ng/mL Activin A (R&D Systems) and 0.1× Knockout Serum Replacement (KSR) (Life Technologies). Media was changed after 24 h and EpiLCs were harvested for RRBS and RNA-seq experiments after 48 h.

For CRISPR-assisted cell line generation, mouse ESCs were maintained on 0.2% gelatin-coated dishes in Dulbecco's modified Eagle's medium (Sigma) supplemented with 16% fetal bovine serum (FBS, Sigma), 0.1 mM ß-mercaptoethanol (Invitrogen), 2 mM L-glutamine (Sigma), 1× MEM Non-essential amino acids (Sigma), 100 U/mL penicillin, 100 µg/mL streptomycin (Sigma), homemade recombinant LIF tested for efficient self-renewal maintenance, and 2i (1 µM PD032591 and 3 µM CHIR99021 (Axon Medchem, Netherlands)).

All cell lines were regularly tested for Mycoplasma contamination by PCR.

Sleeping Beauty Construct

To generate the sleeping beauty donor vector with an N-terminal 3xFLAG tag and a fluorescent readout of doxycycline induction, we first used primers with overhangs harboring SfiI sites to amplify the IRES-DsRed-Express from pIRES2-DsRed-Express (Clontech). This fragment was then cloned into the NruI site in pUC57-GentR via cut-ligation to generate an intermediate cloning vector pUC57-SfiI-IRES-DsRed-Express-SfiI. A synthesized gBlock (IDT, Coralville, IA, USA) containing Kozak-BIO-3XFLAG-AsiSI-NotI-V5 was cloned into the Eco47III site of the intermediate cloning vector via cut-ligation. The luciferase insert from pSBtet-Pur (Kowarz et al., 2015), Addgene plasmid #60507) was excised using SfiI. The SfiI-flanked Kozak-BIO-3XFLAG-AsiSI-NotI-V5-IRES-DsRed-Express cassette was digested out of the intermediate cloning vector using SfiI and ligated into the pSBtet-Pur vector backbone linearized by SfiI. The end result was the parental vector, pSBtet-3xFLAG-IRES-DsRed-Express-PuroR. The *Dppa3* coding sequence was amplified from cDNA using primers with overhangs containing AsiSI and NotI restriction sites and ligated into the parental vector. For experiments involving the SBtet-3xFLAG-*Dppa3* cassette, all inductions were performed using 1 µg/mL doxycycline (Sigma-Aldrich).

CRISPR/Cas9 gene editing and excision

For generation of TET1 catalytic mutants, *Tet1*-specific gRNAs were cloned into a modified version of the SpCas9-T2A-GFP/gRNA (px458;(Ran et al., 2013), Addgene plasmid #48138) or SpCas9-T2A-Puromycin/gRNA vector (px459;(Ran et al., 2013), Addgene plasmid #62988), where we fused truncated human Geminin (hGem) to SpCas9 for increasing homology-directed repair efficiency (Gutschner et al., 2016). A 200 bp ssDNA oligonucleotide harboring the H1652Y and D1654A mutations and ~100 bp of homology to the genomic locus was synthesized (IDT, Coralville, IA, USA). For targetings in wild-type J1 ESCs, cells were transfected with a 4:1 ratio of donor oligo and Cas9/gRNA construct. Positively transfected cells were isolated based on GFP expression using fluorescence-activated cell sorting (FACS) and plated at clonal density in ESC media 2 days after transfection. For the targeting in *Brachyury*$^{GFP/GFP}$ ESCs, cells were plated at clonal density 2 days after transfection and subjected to a transient puromycin selection (1 ug/mL) for 40 h. Colonies were allowed to grow for 6 days, at which point they were picked into 96-well plates, and screened using restriction-fragment length polymorphism (RFLP) analysis. Cell lysis in 96-well plates, PCR on lysates, and restriction digest were

performed as previously described (Mulholland et al., 2015). For all cell lines, *Tet1* catalytic mutation was confirmed by Sanger sequencing.

To generate *Dppa3* knockout cells, the targeting strategy entailed the use of two gRNAs with target sites flanking the *Dppa3* locus to excise the entire locus on both alleles. gRNA oligos were cloned into the SpCas9-T2A-GFP/gRNA vector via cut-ligation. ESCs were transfected with an equimolar amount of each gRNA vector. Two days after transfection, cells were plated at clonal density and subjected to a transient puromycin selection (1 ug/mL) for 40 h. Colonies were picked 6 days after transfection. The triple PCR strategy used for screening is depicted in Figure S6. Briefly, PCR primers 1 and 4 were used to identify clones in which the *Dppa3* locus had been removed, resulting in the appearance of a ~350 bp amplicon. To identify whether the *Dppa3* locus had been removed from both alleles, PCRs were performed with primers 1 and 2 or 3 and 4 to amplify upstream or downstream ends of the *Dppa3* locus, which would only be left intact in the event of mono-allelic locus excision. Removal of the *Dppa3* locus was confirmed with Sanger sequencing and loss of *Dppa3* expression was assessed by qRT-PCR.

Knockout of *Tet1* in *Brachyury*$^{GFP/GFP}$ ESCs was performed as described recently (Mulholland et al., 2018).

For gene editing, all transfections were performed using Lipofectamine 3000 (Thermo Fisher Scientific) according to the manufacturer's instructions. All DNA oligos used for gene editing and screening are listed in Supplementary Table 1.

Bxb1-mediated recombination and Sleeping Beauty Transposition

For the generation of the *Uhrf1*$^{GFP/GFP}$ cell line, we used our previously described ESC line with a C-terminal MIN-tag (*Uhrf1*$^{attP/attP}$*;* Bxb1 *attP* site) and inserted the GFP coding sequence as described previously (Mulholland et al., 2015). Briefly, attB-GFP-Stop-PolyA (Addgene plasmid #65526) was inserted into the C-terminal of the endogenous *Uhrf1*$^{attP/attP}$ locus by transfection with equimolar amounts of Bxb1 and attB-GFP-Stop-PolyA construct, followed by collection of GFP-positive cells with FACS after 6 days.

To generate stable cell lines carrying doxycycline inducible *Dppa3*, cells were first transfected with equimolar amounts of the pSBtet-3xFLAG-Dppa3-IRES-DsRed-PuroR and Sleeping Beauty transposase pCMV(CAT)T7-SB100(Mátés et al., 2009), Addgene plasmid #34879) vector using Lipofectamine 3000 (Thermo Fisher Scientific) according to manufacturer's instructions. Two days after transfection, cells were plated at clonal density and subjected to puromycin selection (1 ug/mL) for 5-6 days. To ensure comparable levels of *Dppa3* induction, cells were first treated for 18 h with doxycycline (1 µg/mL) and then sorted with FACS based on thresholded levels of DsRed expression, the fluorescent readout of successful induction. Post sorting, cells were plated back into media without doxycycline for 7 days before commencing experiments.

Cellular fractionation and Western Blot

Western blot for T1CM ESCs were performed as described previously (Mulholland et al., 2015) using monoclonal antibody rat anti-TET1 5D6 (1:10)(Bauer et al., 2015) and polyclonal rabbit anti-H3 (1:5,000; ab1791, Abcam) as loading control. Blots were probed with secondary antibodies goat anti-rat (1:5,000; 112-035-068, Jackson ImmunoResearch) and goat anti-rabbit (1:5,000; 170–6515, Bio-Rad) conjugated to horseradish peroxidase (HRP) and visualized using an ECL detection kit (Thermo Scientific Pierce).

Cell fractionation was performed as described previously with minor modifications (Méndez and Stillman, 2000). 1×10^7 ESCs were resuspended in 250 µL of buffer A (10 mM HEPES pH 7.9, 10 mM KCl, 1.5 mM $MgCl_2$, 0.34 M sucrose, 10% glycerol, 0.1% Triton X-100, 1 mM DTT, 1 mM phenylmethylsulfonyl fluoride (PMSF), 1x mammalian protease inhibitor cocktail (PI; Roche)) and incubated for 5 min on ice. Nuclei were collected by centrifugation (4 min, 1,300 × g, 4 °C) and the cytoplasmic fraction (supernatant) was cleared again by centrifugation (15 min, 20,000 × g, 4 °C). Nuclei were washed once with buffer A, and then lysed in buffer B (3 mM EDTA, 0.2 mM EGTA, 1 mM DTT, 1 mM PMSF, 1x PI). Insoluble chromatin was collected by centrifugation (4 min, 1,700 × g, 4 °C) and washed once with buffer B. Chromatin fraction was lysed with 1x Laemmli buffer and boiled (10 min, 95°C).

As markers of cytoplasmic and chromatin fractions, alpha-tubulin and histone H3 were detected using monoclonal antibody (mouse anti-alpha-Tubulin, Sigma T9026) and polyclonal antibody (rabbit anti-H3, Abcam ab1791). UHRF1 was visualized by rabbit anti-UHRF1 antibody (Citterio et al., 2004). Western blots for DNMT1 were performed as described previously using a monoclonal antibody (rat anti-DNMT1, 14F6)(Mulholland et al., 2015). GFP and FLAG tagged proteins were visualized by mouse anti-GFP (Roche) and anti-FLAG M2 antibodies (Sigma, F3165), respectively.

Quantitative real-time PCR (qRT-PCR) Analysis

Total RNA was isolated using the NucleoSpin Triprep Kit (Macherey-Nagel) according to the manufacturer's instructions. cDNA synthesis was performed with the High-Capacity cDNA Reverse Transcription Kit (with RNase Inhibitor; Applied Biosystems) using 500 ng of total RNA as input. qRT-PCR assays with oligonucleotides listed in Supplementary Table 1 were performed in 8 µL reactions with 1.5 ng of cDNA used as input. FastStart Universal SYBR Green Master Mix (Roche) was used for SYBR green detection. The reactions were run on a LightCycler480 (Roche).

LC-MS/MS analysis of DNA samples

Isolation of genomic DNA was performed according to earlier published work (Pfaffeneder et al., 2014).

1.0–5 µg of genomic DNA in 35 µL H_2O were digested as follows: 1) An aqueous solution (7.5 µL) of 480 µM $ZnSO_4$, containing 18.4 U nuclease S1 (Aspergillus oryzae, Sigma-Aldrich), 5 U Antarctic phosphatase (New England BioLabs) and labeled internal standards were added ([$^{15}N_2$]-cadC 0.04301 pmol, [$^{15}N_2$,D_2]-hmdC 7.7 pmol, [D_3]-mdC 51.0 pmol, [$^{15}N_5$]-8-oxo-dG 0.109 pmol, [$^{15}N_2$]-fdC 0.04557 pmol) and the mixture was incubated at 37 °C for 3 h. After addition of 7.5 µl of a 520 µM [Na]$_2$-EDTA solution, containing 0.2 U snake venom phosphodiesterase I (Crotalus adamanteus, USB corporation), the sample was incubated for 3 h at 37 °C and then stored at –20 °C. Prior to LC/MS/MS analysis, samples were filtered by using an AcroPrep Advance 96 filter plate 0.2 µm Supor (Pall Life Sciences).

Quantitative UHPLC-MS/MS analysis of digested DNA samples was performed using an Agilent 1290 UHPLC system equipped with a UV detector and an Agilent 6490 triple quadrupole mass spectrometer. Natural nucleosides were quantified with the stable isotope dilution technique. An improved method, based on earlier published work (Pfaffeneder et al., 2014; Wagner et al., 2015) was developed, which allowed the concurrent analysis of all nucleosides in one single analytical run. The source-dependent parameters were as follows: gas temperature 80 °C, gas flow 15 L/min (N_2), nebulizer 30 psi, sheath gas heater 275 °C, sheath gas flow 15 L/min

(N_2), capillary voltage 2,500 V in the positive ion mode, capillary voltage –2,250 V in the negative ion mode and nozzle voltage 500 V. The fragmentor voltage was 380 V/ 250 V. Delta EMV was set to 500 V for the positive mode. Chromatography was performed by a Poroshell 120 SB-C8 column (Agilent, 2.7 µm, 2.1 mm × 150 mm) at 35 °C using a gradient of water and MeCN, each containing 0.0085% (v/v) formic acid, at a flow rate of 0.35 mL/min: 0 →4 min; 0 →3.5% (v/v) MeCN; 4 →6.9 min; 3.5 →5% MeCN; 6.9 →7.2 min; 5 →80% MeCN; 7.2 →10.5 min; 80% MeCN; 10.5 →11.3 min; 80 →0% MeCN; 11.3 →14 min; 0% MeCN. The effluent up to 1.5 min and after 9 min was diverted to waste by a Valco valve. The autosampler was cooled to 4 °C. The injection volume was amounted to 39 µL. Data were processed according to earlier published work (Pfaffeneder et al., 2014).

Flow cytometry analysis

For flow cytometry, plates were washed once with PBS, dissociated to single cells by trypsin-EDTA treatment, resuspended in 2% FBS 1 mM EDTA PBS buffer, and incubated with DyLight 650-conjugated anti SSEA-1 (clone MC-480, MA1-022-D650, Life Technologies) antibody for 30-60 min on ice. Cells were spun down, resuspended in buffer containing DAPI blue for live-dead cell staining and analyzed using a FACS Aria II (BD Biosciences). Cell debris were excluded by forward and side scatter gating. FlowJo was used for data analysis.

RNA-seq and Reduced Representation Bisulfite Sequencing (RRBS)

For RNA-seq, RNA was isolated using the NucleoSpin Triprep Kit (Machery-Nagel) according to the manufacturer's instructions. Digital gene expression libraries for RNA-seq were produced using a modified version of single-cell RNA barcoding sequencing (SCRB-seq) optimized to accommodate bulk cells (Ziegenhain et al., 2017) in which a total of 70 ng of input RNA was used for the reverse-transcription of individual samples. For RRBS, genomic DNA was isolated using the QIAamp DNA Mini Kit (QIAGEN), after an overnight lysis and proteinase K treatment. RRBS library preparation was performed as described previously (Boyle et al., 2012), with the following modifications: bisulfite treatment was performed using the EZ DNA Methylation-Gold™ Kit (Zymo Research Corporation) according to the manufacturer's protocol except libraries were eluted in 2 x 20 µL M-elution buffer. RNA-seq and RRBS libraries were sequenced on on an Illumina HiSeq 1500.

Targeted Bisulfite Amplicon (TaBA) Sequencing

Genomic DNA was isolated from 10^6 cells using the PureLink Genomic DNA Mini Kit (Thermo Fisher Scientific) according to the manufacturer's instructions. The EZ DNA Methylation-Gold Kit (Zymo Research) was used for bisulfite conversion according to the manufacturer's instructions with 500 ng of genomic DNA used as input and the modification that bisulfite converted DNA was eluted in 2 x 20 µL Elution Buffer.

The sequences of the locus specific primers (Supplementary Table 1) were appended with Illumina TruSeq and Nextera compatible overhangs. The amplification of bisulfite converted DNA was performed in 25 µL PCR reaction volumes containing 0.4 µM each of forward and reverse primers, 2 mM Betaine (Sigma-Aldrich, B0300-1VL), 10 mM Tetramethylammonium chloride solution (Sigma-Aldrich T3411-500ML), 1x MyTaq Reaction Buffer, 0.5 units of MyTaq HS (Bioline, BIO-21112), and 1 µL of the eluted bisulfite converted DNA (~12.5 ng). The following cycling parameters were used: 5 min for 95 °C for initial denaturation and activation of the polymerase, 40 cycles (95 °C for 20 s, 58 °C for 30 s, 72 °C for 25 s) and a final elongation at 72 °C for 3 min. Agarose gel electrophoresis was used to determine the quality and yield of the PCR.

For purifying amplicon DNA, PCR reactions were incubated with 1.8x volume of CleanPCR beads (CleanNA, CPCR-0005) for 10 min. Beads were immobilized on a DynaMag™-96 Side Magnet (Thermo Fisher, 12331D) for 5 min, the supernatant was removed, and the beads washed 2x with 150 µL 70% ethanol. After air drying the beads for 5 min, DNA was eluted in 15 µL of 10 mM Tris-HCl pH 8.0. Amplicon DNA concentration was determined using the Quant-iT™ PicoGreen™ dsDNA Assay Kit (Thermo Fisher, P7589) and then diluted to 0.7 ng/µL. Thereafter, indexing PCRs were performed in 25 µL PCR reaction volumes containing 0.08 µM (1 µL of a 2 µM stock) each of i5 and i7 Indexing Primers, 1x MyTaq Reaction Buffer, 0.5 units of MyTaq HS (Bioline, BIO-21112), and 1 µL of the purified PCR product from the previous step. The following cycling parameters were used: 5 min for 95 °C for initial denaturation and activation of the polymerase, 40 cycles (95 °C for 10 s, 55 °C for 30 s, 72 °C for 40 s) and a final elongation at 72 °C for 5 min. Agarose gel electrophoresis was used to determine the quality and yield of the PCR. An aliquot from each indexing reaction (5 µL of each reaction) was then pooled and purified with CleanPCR magnetic beads as described above and eluted in 1 µL x Number of pooled reactions. Concentration of the final library was determined using PicoGreen and the quality and size distribution of the library was assessed with a Bioanalyzer. Dual indexed TaBA-seq libraries were sequenced on an Illumina MiSeq in 2x300 bp output mode.

RNA-seq processing and analysis

RNA-seq libraries were processed and mapped to the mouse genome (mm10) using the zUMIs pipeline (Parekh et al., 2017). UMI count tables were filtered for low counts using HTSFilter (Rau et al., 2013). Differential expression analysis was performed in R using DESeq2(Love et al., 2014) and genes with an adjusted $P<0.05$ were considered to be differentially expressed. Hierarchical clustering was performed on genes differentially expressed in T1KO and T1CM at ESC and EpiLC stage, respectively, using k-means clustering (k=4) in combination with the ComplexHeatmap R-package (Gu et al., 2016). Principal component analysis was restricted to genes differentially expressed during wild-type differentiation and performed using all replicates of wild-type, T1KO and T1CM ESCs and EpiLCs.

RRBS alignment and analysis

Raw RRBS reads were first trimmed using Trim Galore (v.0.3.1) with the '--rrbs' parameter. Alignments were carried out to the mouse genome (mm10) using bsmap (v.2.90) using the parameters '-s 12 -v 10 -r 2 -I 1'. CpG-methylation calls were extracted from the mapping output using bsmaps methratio.py. Analysis was restricted to CpG with a coverage >10. methylKit (Akalin et al., 2012) was used to identify differentially methylated regions between the respective contrasts for the following genomic features: 1) all 1-kb tiles (containing a minimum of three CpGs) detected by RRBS; 2) Repeats (defined by Repbase); 3) gene promoters (defined as gene start sites –2kb/+2kb); and 3) gene bodies (defined as longest isoform per gene) and CpG islands (as defined by (Illingworth et al., 2010)). Differentially methylated regions were identified as regions with $P< 0.05$ and a difference in methylation means between two groups greater than 20%. Principal component analysis of global DNA methylation profiles was performed on single CpGs using all replicates of wild-type, T1KO and T1CM ESCs and EpiLCs.

Chromatin immunoprecipitation (ChIP) and Hydroxymethylated-DNA immunoprecipitation (hMeDIP)

alignment and analysis.

ChIP–seq reads for TET1 binding in ESCs and EpiLCs were downloaded from GSE57700(Xiong et al., 2016) and PRJEB19897(Khoueiry et al., 2017), respectively. hMeDIP reads for wild-type ESCs and T1KO ESCs were download from PRJEB13096(Khoueiry et al., 2017). Reads were aligned to the mouse genome (mm10) with Bowtie (v.1.2.2) with parameters '-a -m 3 -n 3 --best --strata'. Subsequent ChIP–seq analysis was carried out on data of merged replicates. Peak calling and signal pile up was performed using MACS2 callpeak (Zhang et al., 2008) with the parameters '--extsize 150' for ChIP, '--extsize 220' for hMeDIP, and '--nomodel -B --nolambda' for all samples. Tag densities for promoters and 1kb Tiles were calculated using the deepTools2 computeMatrix module (Ramírez et al., 2016). TET1 bound genes were defined by harboring a TET1 peak in the promoter region (defined as gene start sites –2kb/+2kb).

Immunofluorescence staining

For immunostaining, naïve ESCs were grown on coverslips coated with Geltrex (Life Technologies) diluted 1:100 in DMEM/F12 (Life Technologies), thereby allowing better visualization of the cytoplasm during microscopic analysis. All steps during immunostaining were performed at room temperature. Coverslips were rinsed two times with PBS (pH 7.4; 140 mM NaCl, 2.7 mM KCl, 6.5 mM Na_2HPO_4, 1.5 mM KH_2PO_4) prewarmed to 37°C, cells fixed for 10 min with 4% paraformaldehyde (pH 7.0; prepared from paraformaldehyde powder (Merck) by heating in PBS up to 60°C; store at -20°C), washed three times for 10 min with PBST (PBS, 0.01% Tween20), permeabilized for 5 min in PBS supplemented with 0.5% Triton X-100, and washed two times for 10 min with PBS. Primary and secondary antibodies were diluted in blocking solution (PBST, 4% BSA). Coverslips were incubated with primary and secondary antibody solutions in dark humid chambers for 1 h and washed three times for 10 min with PBST after primary and secondary antibodies. For DNA counterstaining, coverslips were incubated 6 min in PBST containing a final concentration of 2 µg/mL DAPI (Sigma-Aldrich) and washed three times for 10 min with PBST. Coverslips were mounted in antifade medium (Vectashield, Vector Laboratories) and sealed with colorless nail polish.

Following primary antibodies were used: polyclonal rabbit anti-DPPA3 (1:200; ab19878, Abcam) and monoclonal rabbit anti-UHRF1 (1:250; D6G8E, Cell Signaling). Following secondary antibodies were used: polyclonal donkey anti-rabbit conjugated to Alexa 488 (1:500; 711-547-003, Dianova), polyclonal donkey anti-rabbit conjugated to Alexa 555 (1:500; A31572, Invitrogen), and polyclonal donkey anti-rabbit conjugated to DyLight fluorophore 594 (1:500; 711-516-152, Dianova). UHRF1-GFP was stained with GFP-Booster ATTO488 (1:200; ChromoTek).

Microscopy and Fluorescence Recovery After Photobleaching (FRAP)

For immunofluorescence, stacks of optical sections were collected on a Nikon TiE microscope equipped with a Yokogawa CSU-W1 spinning disk confocal unit (50 µm pinhole size), an Andor Borealis illumination unit, Andor ALC600 laser beam combiner (405nm/488nm/561nm/640nm), Andor IXON 888 Ultra EMCCD camera, and a Nikon 100x/1.45 NA oil immersion objective. The microscope was controlled by software from Nikon (NIS Elements, ver. 5.02.00). DAPI or fluorophores were excited with 405 nm, 488 nm, or 561 nm laser lines and bright-field images acquired using Nikon differential interference contrast optics. Confocal image z-stacks were recorded with a step size of 200 nm, 16-bit image depth, 1x1 binning, a frame size of 1024×1024 pixels, and a pixel size of 130 nm. Within each experiment, cells were imaged using the same settings on the microscope

(camera exposure time, laser power, and gain) to compare signal intensities between cell lines. Fiji software (ImageJ 1.51j)(Schindelin et al., 2012; Schneider et al., 2012) was used to analyze images and create RGB stacks.

For live-cell imaging, cells were plated on Geltrex-coated glass bottom 2-well imaging slides (Ibidi), allowing to image multiple conditions in parallel. Timelapse images were carried out on the Nikon spinning disk system described above, in an environmental chamber maintained at 37°C with 5% CO_2 (Oko Labs), using a 60x/1.49 NA oil immersion objective and a Perfect Focus System (Nikon). Images were acquired every 10 or 15 min over the course of 12-24 h, with the 488 and 561 nm laser lines, full-frame with 1x1 binning, and with a pixel size of 216 nm. Transfection of a RFP-PCNA vector (Sporbert et al., 2005) was used to identify cells in S-phase. For DNA staining in live cells, cells were grown in media containing 200 nM SiR-DNA (Spirochrome) for 1 h before imaging.

For FRAP assays, cells were imaged in an environmental chamber maintained at 37°C with 5% CO_2 on an Ultraview-Vox spinning disk system (Perkin-Elmer) including a FRAP Photokinesis device mounted to an inverted Axio Observer D1 microscope (Zeiss) equipped with an EMCCD camera (Hamamatsu) and a 63x/1.4 NA oil immersion objective, as well as 405, 488 and 561 nm laser lines. Dox-induced cells or cells in S-phase were found using the 561 nm laser to excite DsRed or RFP-PCNA. Three to four pre-bleach images were acquired with the 488 nm laser, after which a spot (~1 µm) within cells was bleached for 50 ms with a focused 488 nm laser to bleach a fraction of GFP-tagged molecules, and then recovery images were acquired every 2 s for 1 - 2 min. For DNMT1 trapping assays, cells were treated with 30 µM 5-azadeoxycytidine (5-aza-dC) for 1 h prior to FRAP. Recovery analysis was performed in Fiji. Briefly, fluorescence intensity at the bleached spot was measured in background-subtracted images, then normalized to pre-bleach intensity of the bleached spot, and normalized again to the total nuclear intensity in order to account for acquisition photobleaching. Images of cells with visible drift were discarded.

Image Correlation analysis

The characteristic area occupied by fluorescently labeled proteins in cells was determined using a spatial autocorrelation function (SACF), as used in image correlation spectroscopy methods, previously described in (Görisch et al., 2005; Petersen et al., 1993). A two-dimensional SACF was calculated for each frame of a multipoint timelapse image stack in Fiji (Schindelin et al., 2012; Schneider et al., 2012) using a fast fourier transform-based plugin (stack FFT ICS jru v1, by Jay Unruh, available at the Stowers Institute website). Spinning disk images were acquired at relatively low magnification, (60x objective with 216 nm pixels) and all pixels from the whole frame were used for the ACF calculation, without selection or thresholding. As a result, the SACF largely reflects the lengths of predominant fluctuations in fluorescence intensity from the average intensity of the whole frame, which in this case, primarily results in correlation widths roughly the size of the nucleus, or of the whole cell, depending on the distribution of the fluorescent signal. The correlation values from the origin and along both the x- and y- axes were averaged in order to generate a plot profile of the autocorrelation function, and the half-width half-max value (HWHM) was calculated empirically. The HWHM, or correlation width, which gives a readout for the spatial distribution of fluorescence, was then averaged between different fields of view from a multipoint image data set, and plotted over time. A sigmoidal function was fit to the averaged data points

for datasets where doxycycline was added during the time lapse imaging.

Statistics and reproducibility

No statistical methods were used to predetermine sample size, the experiments were not randomized, and the investigators were not blinded to allocation during experiments and outcome assessment. All statistical tests are clearly described in the figure legends and/or in the Methods section, and P values values or adjusted P values are given where possible. For all RRBS experiments, data are derived from n = 2 biological replicates. For Amplicon bisulfite sequencing of LINE-1 elements n = 2 biological replicates were analyzed. For all RNA-seq experiments n = 4 biological replicates corresponding to n = 2 independently cultured samples from 2 clones (T1KO and T1CM) or 4 independently cultured samples (wild-type) were used. QPCR was performed on n = 2 biological replicates (Figure S3f). LC-MS/MS quantification (Figure 3e) was performed on n =4 biological replicates corresponding to n = 2 independently cultured samples from 2 clones (Dppa3KO and T1CM) or 4 independently cultured samples (wild-type).

Data availability

Sequencing data reported in this paper are available at ArrayExpress (EMBL-EBI) under accessions E-MTAB-6785 (wild-type, T1KO, and T1CM RRBS), E-MTAB-6797 (RNA-seq), E-MTAB-6800 (Dppa3KO RRBS). Differential expression analysis is available as tabulated text file in Supplementary Table 2-5 and cluster definitions used in Figure 3 are available in Supplementary Table 6 and 7.

References

Akalin, A., Kormaksson, M., Li, S., Garrett-Bakelman, F.E., Figueroa, M.E., Melnick, A., and Mason, C.E. (2012). methylKit: a comprehensive R package for the analysis of genome-wide DNA methylation profiles. Genome Biol. *13*, R87.

Amouroux, R., Nashun, B., Shirane, K., Nakagawa, S., Hill, P.W., D'Souza, Z., Nakayama, M., Matsuda, M., Turp, A., Ndjetehe, E., et al. (2016). De novo DNA methylation drives 5hmC accumulation in mouse zygotes. Nat. Cell Biol. *18*, 225–233.

Bauer, C., Göbel, K., Nagaraj, N., Colantuoni, C., Wang, M., Müller, U., Kremmer, E., Rottach, A., and Leonhardt, H. (2015). Phosphorylation of TET proteins is regulated via O-GlcNAcylation by the O-linked N-acetylglucosamine transferase (OGT). J. Biol. Chem. *290*, 4801–4812.

Blaschke, K., Ebata, K.T., Karimi, M.M., Zepeda-Martínez, J.A., Goyal, P., Mahapatra, S., Tam, A., Laird, D.J., Hirst, M., Rao, A., et al. (2013). Vitamin C induces Tet-dependent DNA demethylation and a blastocyst-like state in ES cells. Nature *500*, 222–226.

Bostick, M., Kim, J.K., Estève, P.-O., Clark, A., Pradhan, S., and Jacobsen, S.E. (2007). UHRF1 plays a role in maintaining DNA methylation in mammalian cells. Science *317*, 1760–1764.

Boyle, P., Clement, K., Gu, H., Smith, Z.D., Ziller, M., Fostel, J.L., Holmes, L., Meldrim, J., Kelley, F., Gnirke, A., et al. (2012). Gel-free multiplexed reduced representation bisulfite sequencing for large-scale DNA methylation profiling. Genome Biol. *13*, R92.

Carlson, L.L., Page, A.W., and Bestor, T.H. (1992). Properties and localization of DNA methyltransferase in preimplantation mouse embryos: implications for genomic imprinting. Genes Dev. *6*, 2536–2541.

Chen, Q., Chen, Y., Bian, C., Fujiki, R., and Yu, X. (2013). TET2 promotes histone O-GlcNAcylation during gene transcription. Nature *493*, 561–564.

Citterio, E., Papait, R., Nicassio, F., Vecchi, M., Gomiero, P., Mantovani, R., Di Fiore, P.P., and Bonapace, I.M.

(2004). Np95 is a histone-binding protein endowed with ubiquitin ligase activity. Mol. Cell. Biol. *24*, 2526–2535.

Fehling, H.J., Lacaud, G., Kubo, A., Kennedy, M., Robertson, S., Keller, G., and Kouskoff, V. (2003). Tracking mesoderm induction and its specification to the hemangioblast during embryonic stem cell differentiation. Development *130*, 4217–4227.

Ficz, G., Branco, M.R., Seisenberger, S., Santos, F., Krueger, F., Hore, T.A., Marques, C.J., Andrews, S., and Reik, W. (2011). Dynamic regulation of 5-hydroxymethylcytosine in mouse ES cells and during differentiation. Nature *473*, 398–402.

Ficz, G., Hore, T.A., Santos, F., Lee, H.J., Dean, W., Arand, J., Krueger, F., Oxley, D., Paul, Y.-L., Walter, J., et al. (2013). FGF signaling inhibition in ESCs drives rapid genome-wide demethylation to the epigenetic ground state of pluripotency. Cell Stem Cell *13*, 351–359.

Funaki, S., Nakamura, T., Nakatani, T., Umehara, H., Nakashima, H., and Nakano, T. (2014). Inhibition of maintenance DNA methylation by Stella. Biochem. Biophys. Res. Commun. *453*, 455–460.

Görisch, S.M., Wachsmuth, M., Tóth, K.F., Lichter, P., and Rippe, K. (2005). Histone acetylation increases chromatin accessibility. J. Cell Sci. *118*, 5825–5834.

Gu, Z., Eils, R., and Schlesner, M. (2016). Complex heatmaps reveal patterns and correlations in multidimensional genomic data. Bioinformatics *32*, 2847–2849.

Gutschner, T., Haemmerle, M., Genovese, G., Draetta, G.F., and Chin, L. (2016). Post-translational Regulation of Cas9 during G1 Enhances Homology-Directed Repair. Cell Rep. *14*, 1555–1566.

Habibi, E., Brinkman, A.B., Arand, J., Kroeze, L.I., Kerstens, H.H.D., Matarese, F., Lepikhov, K., Gut, M., Brun-Heath, I., Hubner, N.C., et al. (2013). Whole-genome bisulfite sequencing of two distinct interconvertible DNA methylomes of mouse embryonic stem cells. Cell Stem Cell *13*, 360–369.

Hashimoto, H., Horton, J.R., Zhang, X., Bostick, M., Jacobsen, S.E., and Cheng, X. (2008). The SRA domain of UHRF1 flips 5-methylcytosine out of the DNA helix. Nature *455*, 826–829.

Hayashi, K., and Saitou, M. (2013). Generation of eggs from mouse embryonic stem cells and induced pluripotent stem cells. Nat. Protoc. *8*, 1513–1524.

Hayashi, K., de Sousa Lopes, S.M.C., Tang, F., Lao, K., and Surani, M.A. (2008). Dynamic equilibrium and heterogeneity of mouse pluripotent stem cells with distinct functional and epigenetic states. Cell Stem Cell *3*, 391–401.

Hayashi, K., Ohta, H., Kurimoto, K., Aramaki, S., and Saitou, M. (2011). Reconstitution of the mouse germ cell specification pathway in culture by pluripotent stem cells. Cell *146*, 519–532.

Hill, P.W.S., Leitch, H.G., Requena, C.E., Sun, Z., Amouroux, R., Roman-Trufero, M., Borkowska, M., Terragni, J., Vaisvila, R., Linnett, S., et al. (2018). Epigenetic reprogramming enables the transition from primordial germ cell to gonocyte. Nature *555*, 392–396.

Illingworth, R.S., Gruenewald-Schneider, U., Webb, S., Kerr, A.R.W., James, K.D., Turner, D.J., Smith, C., Harrison, D.J., Andrews, R., and Bird, A.P. (2010). Orphan CpG islands identify numerous conserved promoters in the mammalian genome. PLoS Genet. *6*, e1001134.

Ito, S., Shen, L., Dai, Q., Wu, S.C., Collins, L.B., Swenberg, J.A., He, C., and Zhang, Y. (2011). Tet proteins can convert 5-methylcytosine to 5-formylcytosine and 5-carboxylcytosine. Science *333*, 1300–1303.

Khoueiry, R., Sohni, A., Thienpont, B., Luo, X., Velde, J.V., Bartoccetti, M., Boeckx, B., Zwijsen, A., Rao, A., Lambrechts, D., et al. (2017). Lineage-specific functions of TET1 in the postimplantation mouse embryo. Nat. Genet.

Koh, K.P., Yabuuchi, A., Rao, S., Huang, Y., Cunniff, K., Nardone, J., Laiho, A., Tahiliani, M., Sommer, C.A., Mostoslavsky, G., et al. (2011). Tet1 and Tet2 regulate 5-hydroxymethylcytosine production and cell lineage

specification in mouse embryonic stem cells. Cell Stem Cell *8*, 200–213.

Kowarz, E., Löscher, D., and Marschalek, R. (2015). Optimized Sleeping Beauty transposons rapidly generate stable transgenic cell lines. Biotechnol. J. *10*, 647–653.

Leeb, M., Dietmann, S., Paramor, M., Niwa, H., and Smith, A. (2014). Genetic exploration of the exit from self-renewal using haploid embryonic stem cells. Cell Stem Cell *14*, 385–393.

Love, M.I., Huber, W., and Anders, S. (2014). Moderated estimation of fold change and dispersion for RNA-seq data with DESeq2. Genome Biol. *15*, 550.

Maenohara, S., Unoki, M., Toh, H., Ohishi, H., Sharif, J., Koseki, H., and Sasaki, H. (2017). Role of UHRF1 in de novo DNA methylation in oocytes and maintenance methylation in preimplantation embryos. PLoS Genet. *13*, e1007042.

Mátés, L., Chuah, M.K.L., Belay, E., Jerchow, B., Manoj, N., Acosta-Sanchez, A., Grzela, D.P., Schmitt, A., Becker, K., Matrai, J., et al. (2009). Molecular evolution of a novel hyperactive Sleeping Beauty transposase enables robust stable gene transfer in vertebrates. Nat. Genet. *41*, 753–761.

Méndez, J., and Stillman, B. (2000). Chromatin association of human origin recognition complex, cdc6, and minichromosome maintenance proteins during the cell cycle: assembly of prereplication complexes in late mitosis. Mol. Cell. Biol. *20*, 8602–8612.

von Meyenn, F., Iurlaro, M., Habibi, E., Liu, N.Q., Salehzadeh-Yazdi, A., Santos, F., Petrini, E., Milagre, I., Yu, M., Xie, Z., et al. (2016). Impairment of DNA Methylation Maintenance Is the Main Cause of Global Demethylation in Naive Embryonic Stem Cells. Mol. Cell.

Mulholland, C.B., Smets, M., Schmidtmann, E., Leidescher, S., Markaki, Y., Hofweber, M., Qin, W., Manzo, M., Kremmer, E., Thanisch, K., et al. (2015). A modular open platform for systematic functional studies under physiological conditions. Nucleic Acids Res. *43*, e112.

Mulholland, C.B., Traube, F.R., Parsa, E., Eckl, E.-M., Schoenung, M., Modic, M., Bartoschek, M.D., Stolz, P., Ryan, J., Carell, T., et al. (2018). Distinct and stage-specific contributions of TET1 and TET2 to stepwise cytosine oxidation in the transition from naive to primed pluripotency.

Nakamura, T., Arai, Y., Umehara, H., Masuhara, M., Kimura, T., Taniguchi, H., Sekimoto, T., Ikawa, M., Yoneda, Y., Okabe, M., et al. (2007). PGC7/Stella protects against DNA demethylation in early embryogenesis. Nat. Cell Biol. *9*, 64–71.

Nakashima, H., Kimura, T., Kaga, Y., Nakatani, T., Seki, Y., Nakamura, T., and Nakano, T. (2013). Effects of dppa3 on DNA methylation dynamics during primordial germ cell development in mice. Biol. Reprod. *88*, 125.

Parekh, S., Ziegenhain, C., Vieth, B., Enard, W., and Hellmann, I. (2017). zUMIs: A fast and flexible pipeline to process RNA sequencing data with UMIs.

Petersen, N.O., Höddelius, P.L., Wiseman, P.W., Seger, O., and Magnusson, K.E. (1993). Quantitation of membrane receptor distributions by image correlation spectroscopy: concept and application. Biophys. J. *65*, 1135–1146.

Pfaffeneder, T., Hackner, B., Truss, M., Münzel, M., Müller, M., Deiml, C.A., Hagemeier, C., and Carell, T. (2011). The discovery of 5-formylcytosine in embryonic stem cell DNA. Angew. Chem. Int. Ed Engl. *50*, 7008–7012.

Pfaffeneder, T., Spada, F., Wagner, M., Brandmayr, C., Laube, S.K., Eisen, D., Truss, M., Steinbacher, J., Hackner, B., Kotljarova, O., et al. (2014). Tet oxidizes thymine to 5-hydroxymethyluracil in mouse embryonic stem cell DNA. Nat. Chem. Biol. *10*, 574–581.

Ramírez, F., Ryan, D.P., Grüning, B., Bhardwaj, V., Kilpert, F., Richter, A.S., Heyne, S., Dündar, F., and Manke, T. (2016). deepTools2: a next generation web server for deep-sequencing data analysis. Nucleic Acids Res. *44*, W160–W165.

Ran, F.A., Hsu, P.D., Wright, J., Agarwala, V., Scott, D.A., and Zhang, F. (2013). Genome engineering using the

CRISPR-Cas9 system. Nat. Protoc. *8*, 2281–2308.

Rau, A., Gallopin, M., Celeux, G., and Jaffrézic, F. (2013). Data-based filtering for replicated high-throughput transcriptome sequencing experiments. Bioinformatics *29*, 2146–2152.

Sato, M., Kimura, T., Kurokawa, K., Fujita, Y., Abe, K., Masuhara, M., Yasunaga, T., Ryo, A., Yamamoto, M., and Nakano, T. (2002). Identification of PGC7, a new gene expressed specifically in preimplantation embryos and germ cells. Mech. Dev. *113*, 91–94.

Schermelleh, L., Spada, F., Easwaran, H.P., Zolghadr, K., Margot, J.B., Cardoso, M.C., and Leonhardt, H. (2005). Trapped in action: direct visualization of DNA methyltransferase activity in living cells. Nat. Methods *2*, 751–756.

Schindelin, J., Arganda-Carreras, I., Frise, E., Kaynig, V., Longair, M., Pietzsch, T., Preibisch, S., Rueden, C., Saalfeld, S., Schmid, B., et al. (2012). Fiji: an open-source platform for biological-image analysis. Nat. Methods *9*, 676–682.

Schneider, C.A., Rasband, W.S., and Eliceiri, K.W. (2012). NIH Image to ImageJ: 25 years of image analysis. Nat. Methods *9*, 671–675.

Seisenberger, S., Andrews, S., Krueger, F., Arand, J., Walter, J., Santos, F., Popp, C., Thienpont, B., Dean, W., and Reik, W. (2012). The dynamics of genome-wide DNA methylation reprogramming in mouse primordial germ cells. Mol. Cell *48*, 849–862.

Sharif, J., Muto, M., Takebayashi, S.-I., Suetake, I., Iwamatsu, A., Endo, T.A., Shinga, J., Mizutani-Koseki, Y., Toyoda, T., Okamura, K., et al. (2007). The SRA protein Np95 mediates epigenetic inheritance by recruiting Dnmt1 to methylated DNA. Nature *450*, 908–912.

Shen, L., Inoue, A., He, J., Liu, Y., Lu, F., and Zhang, Y. (2014). Tet3 and DNA replication mediate demethylation of both the maternal and paternal genomes in mouse zygotes. Cell Stem Cell *15*, 459–471.

Sporbert, A., Domaing, P., Leonhardt, H., and Cardoso, M.C. (2005). PCNA acts as a stationary loading platform for transiently interacting Okazaki fragment maturation proteins. Nucleic Acids Res. *33*, 3521–3528.

Szwagierczak, A., Bultmann, S., Schmidt, C.S., Spada, F., and Leonhardt, H. (2010). Sensitive enzymatic quantification of 5-hydroxymethylcytosine in genomic DNA. Nucleic Acids Res. *38*, e181.

Tahiliani, M., Koh, K.P., Shen, Y., Pastor, W.A., Bandukwala, H., Brudno, Y., Agarwal, S., Iyer, L.M., Liu, D.R., Aravind, L., et al. (2009). Conversion of 5-methylcytosine to 5-hydroxymethylcytosine in mammalian DNA by MLL partner TET1. Science *324*, 930–935.

Vella, P., Scelfo, A., Jammula, S., Chiacchiera, F., Williams, K., Cuomo, A., Roberto, A., Christensen, J., Bonaldi, T., Helin, K., et al. (2013). Tet proteins connect the O-linked N-acetylglucosamine transferase Ogt to chromatin in embryonic stem cells. Mol. Cell *49*, 645–656.

Waghray, A., Saiz, N., Jayaprakash, A.D., Freire, A.G., Papatsenko, D., Pereira, C.-F., Lee, D.-F., Brosh, R., Chang, B., Darr, H., et al. (2015). Tbx3 Controls Dppa3 Levels and Exit from Pluripotency toward Mesoderm. Stem Cell Reports *5*, 97–110.

Wagner, M., Steinbacher, J., Kraus, T.F.J., Michalakis, S., Hackner, B., Pfaffeneder, T., Perera, A., Müller, M., Giese, A., Kretzschmar, H.A., et al. (2015). Age-dependent levels of 5-methyl-, 5-hydroxymethyl-, and 5-formylcytosine in human and mouse brain tissues. Angew. Chem. Int. Ed Engl. *54*, 12511–12514.

Weber, M., Hellmann, I., Stadler, M.B., Ramos, L., Pääbo, S., Rebhan, M., and Schübeler, D. (2007). Distribution, silencing potential and evolutionary impact of promoter DNA methylation in the human genome. Nat. Genet. *39*, 457–466.

Williams, K., Christensen, J., Pedersen, M.T., Johansen, J.V., Cloos, P.A.C., Rappsilber, J., and Helin, K. (2011). TET1 and hydroxymethylcytosine in transcription and DNA methylation fidelity. Nature *473*, 343–348.

Wu, H., D'Alessio, A.C., Ito, S., Xia, K., Wang, Z., Cui, K., Zhao, K., Sun, Y.E., and Zhang, Y. (2011). Dual

functions of Tet1 in transcriptional regulation in mouse embryonic stem cells. Nature *473*, 389–393.

Xiong, J., Zhang, Z., Chen, J., Huang, H., Xu, Y., Ding, X., Zheng, Y., Nishinakamura, R., Xu, G.-L., Wang, H., et al. (2016). Cooperative Action between SALL4A and TET Proteins in Stepwise Oxidation of 5-Methylcytosine. Mol. Cell *64*, 913–925.

Zhang, Y., Liu, T., Meyer, C.A., Eeckhoute, J., Johnson, D.S., Bernstein, B.E., Nusbaum, C., Myers, R.M., Brown, M., Li, W., et al. (2008). Model-based analysis of ChIP-Seq (MACS). Genome Biol. *9*, R137.

Ziegenhain, C., Vieth, B., Parekh, S., Reinius, B., Guillaumet-Adkins, A., Smets, M., Leonhardt, H., Heyn, H., Hellmann, I., and Enard, W. (2017). Comparative Analysis of Single-Cell RNA Sequencing Methods. Mol. Cell *65*, 631–643.e4.